

Article

Research on Shovel-Force Prediction and Power-Matching Optimization of a Large-Tonnage Electric Wheel Loader

Jiajie Wei, Jiazhi Zhao and Jixin Wang *

School of Mechanical and Aerospace Engineering, Jilin University, Changchun 130025, China; wjj2609@sohu.com (J.W.); zhaojiazhi0726@gmail.com (J.Z.)

* Correspondence: jxwang@jlu.edu.cn

Featured Application: The proposed methods for predicting shovel force and power-matching optimization can enhance the operational efficiency of large-tonnage electric wheel loader.

Abstract: Nowadays, rapid development has been achieved with respect to the electric wheel loader (EWL). The operational efficiency of EWLs is affected by many factors; especially, shovel force is a very important factor. For large-tonnage EWLs, when employing empirical, formula-based methods to predict shovel force, the generated errors are significant, with errors frequently reaching levels of up to 30%. To solve this problem, a method, based on the discrete element method (DEM), to predict shovel force is put forward in this paper. The material parameters are calibrated by a backpropagation (BP) neural network learning algorithm (NNLA). The material model is inputted into multi-body-dynamics software. A simulation model to accurately predict the shovel force is created. The error between the test results and the simulation results is 7.8%, demonstrating a high level of consistency. To validate the reliability of this method, the 35-ton EWL is taken as an example for research, and the straight-line driving test and the power-matching test are conducted. While ensuring the operational efficiency of the EWLs, the power loss is also a crucial consideration. The drastic changes in shovel force often result in front-tire slippage of the EWLs. To minimize wheel slippage during the shoveling section, the matching of the electric motor was optimized. In summary, material parameters were calibrated using a combined method of BP NNLA to predicate shovel force of a large-tonnage EWL. Additionally, the power matching of the EWL has been optimized to accord with the shoveling section of the device.

Keywords: electric wheel loader; shovel force; discrete element method; material calibration; back-propagation neural network learning algorithm



Citation: Wei, J.; Zhao, J.; Wang, J. Research on Shovel-Force Prediction and Power-Matching Optimization of a Large-Tonnage Electric Wheel Loader. *Appl. Sci.* **2023**, *13*, 13324. <https://doi.org/10.3390/app132413324>

Academic Editor: Gang Lei

Received: 9 November 2023

Revised: 9 December 2023

Accepted: 12 December 2023

Published: 17 December 2023



Copyright: © 2023 by the authors. Licensee MDPI, Basel, Switzerland. This article is an open access article distributed under the terms and conditions of the Creative Commons Attribution (CC BY) license (<https://creativecommons.org/licenses/by/4.0/>).

1. Introduction

The large-tonnage EWL is a widely used piece of mining machinery. The large-tonnage EWL is capable of shoveling, transporting, and unloading materials [1]. They are primarily used for handling loose materials, including soil, sand, gravel, and limestone. In recent years, due to operational demands, mining machinery has required higher efficiency levels and loading capacities. Because of advantages in size, bucket capacity, and tonnage, the large-tonnage EWLs have become increasingly popular. The shovel force is a crucial factor influencing the shoveling section of the device [2]. When shoveling materials, the shove force will experience a sharp increase and exhibit abrupt changes. When the shovel force exceeds the ground traction of the EWL, the tires of the EWL will slip, resulting in an additional power loss.

Currently, there are three main methods used to improve the accuracy of bucket-force prediction: theoretical calculation, empirical formula, and discrete-element-based methods. This paper adopts a discrete-element-based approach. Compared to theoretical calculation, the discrete-element-based method makes it easier to obtain test data. In contrast to the

empirical formula, which tends to have larger prediction errors for large-tonnage EWLs, the discrete-element-based method exhibits smaller prediction errors in the estimation of shovel force for large-tonnage EWLs.

During the new-product design period of large-tonnage EWLs, when some data are lacking, it has been observed that using the empirical-formula-based methods to match motor power based on shovel force could result in significant errors. This could have a substantial impact on the EWL's design. To avoid the risk of design failure due to excessively high or low power-matching results, especially when the bucket of EWL configurations is similar, a method based on discrete elements has been proposed. This method selects the most typical operational and material conditions for EWLs, providing a method for accurate prediction of shovel force.

The operational efficiency of EWLs is directly affected by shovel force. The forward design of buckets and engine matching has been guided by the research on shovel force. Therefore, many scholars have conducted extensive research on the loading section. Li Ru [3] selected four factors, with a significant impact given to shovel force. She used orthogonal simulation analysis and range analysis to study the effects of these factors on the force at the peak of the shovel force. The factors were found to have the following order of significance: particle size, bucket width, insertion speed, and particle shape. Chen Yu [4], focusing on conditions associated with the loading of gravel, conducted comparative studies by installing different numbers of bucket teeth. The research found that the number of bucket teeth had an impact of no higher than 10% on shovel force, no higher than 7% on the full bucket rate, and no higher than 3.5% on insertion depth. Ding Zhuang [5] has proposed an improved conformal mapping (ICM) method for analyzing the air-gap magnetic field in surface-mounted permanent magnet synchronous motors (SPMSMs). In comparison to the traditional conformal mapping (TCM) method, ICM demonstrates higher calculation speed and accuracy by reducing the amount of mapping time. The article validates the accuracy and efficiency of the ICM method through an experimental prototype of an eccentric-shaped-pole permanent magnet motor. Yang Ming [6] introduces a multidisciplinary design optimization framework for underwater gliders. The article establishes a universal disciplinary framework and enhances efficiency through approximate models. The proposed approach combines concurrent subspace optimization, a penalty function method, and a multipopulational genetic algorithm. Validated through a sea trial of an improved Petrel-L glider, the method rapidly determines optimal design parameters. Bai Xue [7] proposes a low-thrust reconfiguration strategy for formation flying using Jordan normal form. The article evaluates performance in terms of control acceleration and fuel cost, employing Jordan decomposition to simplify relative dynamics. The trajectory optimization method, based on a functional integral and polynomial series, is analytically proven to be valid. The numerical results demonstrate successful and efficient formation reconfiguration. Shi Maolin [8] introduces ESVR-MFS, a multi-fidelity surrogate model based on extreme support vector regression (ESVR) for engineering system optimization. ESVR-MFS efficiently utilizes both higher-fidelity and lower-fidelity samples, demonstrating competitive performance in terms of prediction accuracy and computational cost. The proposed approach is valuable for practical multi-fidelity engineering design problems. Liu Long [9] has proposed an ammonia–diesel stratified injection technology for the application of low-carbon ammonia fuel in marine engines, aiming to meet future low-carbon emission regulations. The results indicate that this strategy achieves a power output comparable to those of traditional diesel engines, without the need for additional matching pilot fuel injectors, and while significantly reducing CO₂ and NO_x emissions. This innovative approach holds promising prospects for future applications in marine engines. Bai Xiaotian [10] investigated the potential threat posed by subsurface mesoscale cracks in the outer ring of full ceramic ball bearings (FCBBs) to the stable operation of related devices. Using a dynamic model based on the strain energy theory, the study analyzed the impact of different crack lengths on the operational state. Li Tao [11] presents a digital-twin-driven model for predicting early degradation in ceramic bearings. Us-

ing an LSTM neural network and vibration signals, it maps stiffness weakening factors to degradation indices. The model, combining digital-twin technology with real-time data, effectively predicts early degradation trends, offering insights for life-prediction and maintenance strategies for ceramic components in key aviation and military equipment. Liao Kai [12] proposes a low-pass virtual filter (VF) for wind energy conversion systems (WECSs) to smooth power output without the need for a physical energy storage system. The VF, integrated into the active power control loop, effectively reduces high-frequency wind power fluctuations. A stability-constrained coefficient ensures wind turbine (WT) stability. Simulations and experiments validate the VF's efficacy in minimizing wind power fluctuations and the stability-constrained coefficient's role in maintaining WT stability. Li Zhen [13] used objective function optimization theory with the maximum level bucket capacity as the objective function. They optimized the parameters for a high-performance bucket for a 3-ton EWL. Through comprehensive performance experiments, they verified the advantages of the high-performance bucket in terms of operating efficiency, fuel economy, and other aspects. M Zauner [14] places greater emphasis on detecting the impact caused by uneven terrain during vehicle travel, particularly concerning speed control, and extracts roughness coefficients by monitoring actual vertical acceleration caused by uneven terrain. This tactic utilizes a self-supervised learning approach to predict these coefficients from laser data, aiming to facilitate the safe deceleration of vehicles. The key distinction of the present work lies in the fact that this paper focuses on the prediction of shovel force and power-matching optimization for large-tonnage EWLs, emphasizing the optimization of vehicle power matching and control. This paper employs the discrete element method (DEM) and a backpropagation neural network learning algorithm (BP NNLA), combining theoretical analysis and simulation to predict shovel force and optimize power matching.

The design of the bucket and engine matching is guided by the research on shovel force. Many scholars have conducted extensive research on the loading section of the device [15,16]. For small-sized and medium-sized EWLs, shovel force is mainly predicted and analyzed through empirical-formula-based methods. In comparison to small-sized and medium-sized EWLs, large-tonnage EWLs have significant differences in power matching, transmission, tire traction, and other technologies. Empirical-formula-based methods cannot meet the precision requirements of the designs of large-tonnage EWLs. It is necessary to research shovel force under typical conditions for large-tonnage EWLs to increase in operational efficiency. This article contains the following innovative points and contributions.

1. Combining DEM and BP NNLA: A method for accurately predicting shovel force in large-tonnage EWLs is proposed by combining DEM and BP NNLA. The innovation of this method lies in the combination of DEM simulation and BP NNLA learning to enhance the accuracy of the predictions of shovel force in EWLs.
2. Calibration of Material Parameters: Through BP NNLA, the material parameters are calibrated to enhance the reliability of the model. This step involves the systematic analysis and calibration of factors such as material density, Poisson's ratio, shear modulus, etc., making the model more closely aligned with real-world conditions.
3. Accurate Prediction of Shovel Force for Large-Tonnage EWLs: Through simulation methods, an accurate prediction of shovel force for EWLs of various tonnages has been successfully achieved. Compared to traditional empirical formulas, this method improves prediction accuracy, particularly for large-tonnage EWLs, resulting in more reliable forecasting results.
4. Power-Matching Optimization: With the accurate prediction of shovel force, the power matching of EWLs has been optimized, thereby enhancing operational efficiency.

This paper will revolve around two experimental frameworks. Firstly, accurately predicting the shovel force of large-tonnage EWLs, using the DEM and NNLA. Secondly, optimizing the matching and control of EWLs through experiments under different operational conditions.

2. Shovel Force of the Shovel Step in Typical Working Conditions

The actual operating conditions of EWLs include various types of work, including I-type, V-type, and L-type operations. This paper focuses on the most typical V-type operating conditions of EWLs. The steps that the EWL employs in shoveling materials are analyzed in order to investigate the shovel force.

2.1. Analysis of EWL Operational Steps

When EWLs load and unload materials, a typical V-type operating cycle typically consists of the following four steps:

- (1) S1 Shoveling: The EWL's boom is in the lower position. The EWL's bucket is level with the ground, and the distance between the bucket and the lower pivot-point of the boom arm is a certain distance from the ground. With the assistance of the EWL's power, the bucket is horizontally inserted into the material. The shoveling step has been completed. When the shoveling method of the EWL varies, the states of the boom cylinder and bucket cylinder are also different.
- (2) S2 Full-load Transporting: To save time, while transporting materials to the unloading point, the working equipment of the EWL is raised to the desired position. During this step, the boom cylinder of the EWL extends, and the bucket cylinder is in a locked condition.
- (3) S3 Unloading: By operating the bucket cylinder, the material is unloaded into the self-dumping truck. The boom cylinder is in a locked position, and the bucket cylinder retracts.
- (4) S4 No-Load Returning: After unloading is complete, the cylinder is operated in order to lower the boom, and the bucket is made level with the ground. Concurrently, the boom cylinder retracts, and the bucket cylinder extends. The EWL automatically enters the next working cycle. The work-step follows a V-type operating pattern, as shown in Figure 1.

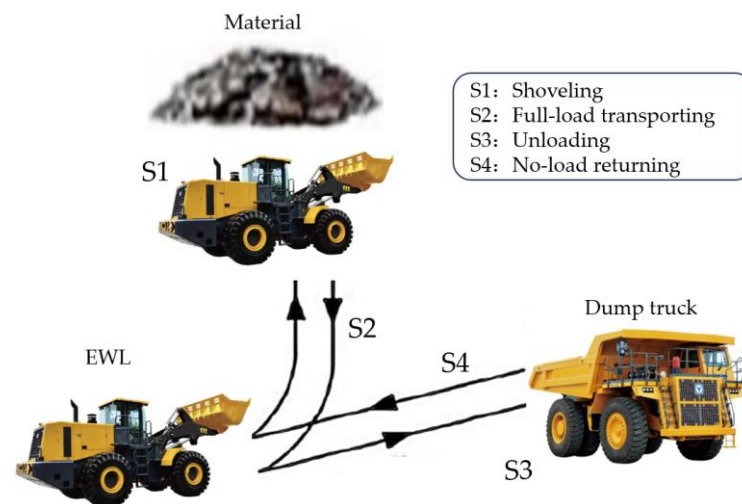


Figure 1. V-type operational cycle of a large-tonnage EWL.

2.2. Empirical Calculation of Shovel Force

The operational efficiency of an EWL is influenced by various factors. During the process of material loading, the loading time of an EWL primarily depends on its power performance. Shovel force is a parameter directly affecting the power performance of the EWL. Previously, shovel force has mainly been predicted by empirical, formula-based methods. The empirical formula for shovel force F is as follows [17]:

$$F = 9.8K_1K_2L^{1.25}BK_3K_4 \quad (1)$$

- K_1 —Impact coefficient of material block size and looseness.
 K_2 —Impact coefficient of material type.
 K_3 —Impact coefficient for the pile height of loose materials.
 K_4 —Impact coefficient of shape (typically ranging from 1.1 to 1.8).
 L —Depth of bucket insertion into the material stack.
 B —Bucket width.

This formula includes multiple parameter-values. The bucket width (B) can be measured. The bucket's insertion depth into the material pile (L) can be determined through experiments [18]. Other parameters need to be established based on empirical values. The method exhibits significant calculation errors. Due to the difficulty in obtaining the parameters in the formula, further discussion is required.

$$L = kL_1 \quad (2)$$

$$K = k_1k_2k_3k_4 \quad (3)$$

- K —Coefficient of composite.
 k —Coefficient of bucket depth.
 L_1 —Depth of bucket.

Based on the test results, the measured shovel force of the 5-ton EWL is 160 kN. The EWL's width (B) is 2.88 m, the bucket depth (L_1) is 1.1407 m, and the bucket's insertion depth into the material pile (L) is 1.156 m. By plugging these values into the above formula, the bucket depth coefficient (k) is determined to be 1.013, and the comprehensive coefficient (K) is 4.7318. The bucket depth coefficient (k) and the comprehensive coefficient (K) have been adjusted based on the measured shovel force from 7-ton, nine-ton, 12-ton, and 15-ton EWLs. Table 1 summarizes the calculated shovel force. From Table 1, the errors of shovel force in the cases of medium-to-small tonnage EWLs (3~12 ton) can be controlled to within 10% or less. There is a larger error of the shovel force for large-tonnage EWLs (15-ton and 35-ton). Using empirical, formula-based methods to predict shovel force is imprecise. New research methods are needed to predicate the shovel force.

Table 1. Comparisons of shovel force.

Type of EWL /ton	Measured Shovel Force/kN	Calculated Shovel Force/kN	Error /%
3	127	136	7.08
5	160	163	1.88
7	207	209	0.96
9	270	265	1.85
12	380	344	9.4
15	420	353	15.9
35	900	700	28.6

3. Review and Application of Dynamic Discrete-Element Method

To understand the reasons for the calculation errors in the shovel force of large-tonnage EWLs, an analysis of shovel force was conducted during the loading and shoveling tasks of the EWL.

3.1. Shovel-Force Analysis

During the shoveling section, EWLs are subjected to shovel force. If this force is not managed properly, there is a risk of tire slippage [19]. Accurately analyzing the shovel force is important. Shovel force can be broadly categorized into three types, including horizontal insertion force, vertical shovel force, and the bucket rotation torque. Due to the complexity of the actual shoveling section, analyzing these forces according to different shoveling scenarios is necessary.

During the entire shoveling section, loaders experience five different forces. $F1$ represents the insertion force. $F2$ is the shovel force at the bucket bottom. $F3$ is the gravity of the materials being loaded. $F4$ accounts for the frictional forces between the loaded material and the inner wall of the bucket (including friction resulting from relative sliding and rolling). $F5$ corresponds to the sliding force on the slip surface [20], as illustrated in Figure 2a.

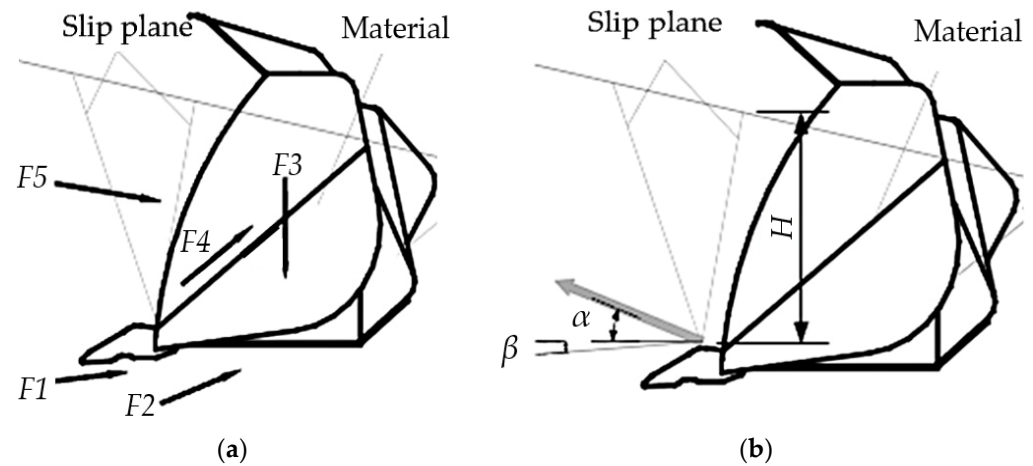


Figure 2. Types of shovel force during shoveling: (a) shovel force distribution; (b) bucket movement direction.

In Figure 2b, the α represents the angle between the movement direction of the EWL and the horizontal plane, the β is the angle between the horizontal direction and the cutting edge of the bucket, and the H is the height of the filled material. Based on geometric and kinematic relationships, the relationship between bucket shoveling volume and the trajectory of EWL can be derived [21]. Expressions for other forces can also be derived. The derivation section requires the use of numerical computations, which can introduce significant errors. The DEM can effectively solve these issues.

3.2. Application of Discrete Element Method

The model of dynamics with DEM involves four steps, including utilizing the BP NNLA to adjust the material parameters, creating the material model with the DEM software, importing the material model into the multi-body-dynamics software to construct the joint simulation model, and analyzing the process of bucket-shoveling materials. To validate the feasibility of model, the simulation results are compared with the results of a 5-ton EWL test. Based on this, other simulation scenarios are conducted.

3.3. Review of BP NNLA

Neural networks are a novel control technology. Neural networks simulate the structure and function of the human brain. Neural network control does not require precise mathematical models. This technology possesses strong autonomous learning, parallel processing, and fault tolerance capabilities. Neural network technology is capable of handling complex and nonlinear problems.

The establishment of the BP neural network structure involves multiple sections, including data collection and preparation, selection of the network structure, model compilation, model training, and adjustment and optimization. Ultimately, the neural network structure is constructed, as described in Reference [22]. In the structure of BP NNLA, i represents the input layer nodes, j represents the hidden layer nodes, and k represents the output layer nodes. The input layer nodes include the recovery coefficient, the static friction coefficient, and the dynamic friction coefficient. The output layer nodes represent the force of the hydraulic cylinder force. The input layer consists of three parameters that

undergo the influence of nodes in hidden layer nodes. A non-linear mapping relationship is established between the input layer nodes and the output layer nodes to predict the value of the hydraulic cylinder force. The model's structure is illustrated in Figure 3.

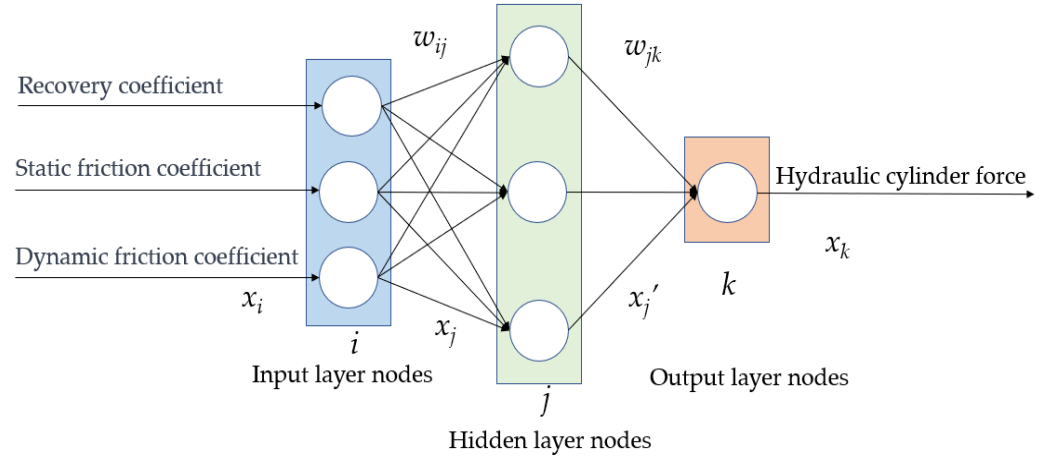


Figure 3. Structure of BP NNLA.

The output of the j -th neuron in the hidden layer nodes is expressed as [22]

$$x_j^l = f\left(\sum_k w_{jk}^l x_k^{l-1} + b_j^l\right) \tag{4}$$

The output of the k -th neuron in the output layer nodes is expressed as

$$x_k = f\left(\sum_j w_{jk}^{L-1} x_j^{L-1} + b_k^{L-1}\right) \tag{5}$$

In the formula, w_{jk}^l represents the weight between the k -th neuron in the $(l-1)$ -th layer and the j -th neuron in the l -th layer. The term b_j^l represents the threshold of the j -th neuron in the l -th layer. L represents the number of layers in the neural network, f represents the transfer function of the hidden layers, and F represents the transfer function of the output layer.

4. Simulation of Shovel Force

The simulation is performed by the DEM. The difficulty lies in defining the key parameters for the simulation. Accurate simulation of key parameters can be obtained through material calibration. To ensure the effectiveness of the simulation, it is necessary to control the error between the simulation's results and the experimental results, keeping it within an acceptable range.

4.1. Material Calibration

4.1.1. Experimental Process

The experiments mainly consist of two parts: static and dynamic calibration experiments [23]. The static calibration experiment involves the measurement of the physical parameters of the loading material. The necessary measurement tools include an inclinometer and a tape measure. These tools are used to measure the on-site ore pile density, particle size, repose angle, and other parameters. The static calibration experiment is depicted in Figure 4.



Figure 4. Static calibration experiment: (a) particle size measurement in ore samples; (b) repose angle measurement in ore samples.

The dynamic calibration experiment involves data collection for the mechanical parameters of the loading section, as shown in Figure 5. The required measurement tools include pressure sensors and GPS devices. Parameters such as cylinder displacement, oil pressure, and EWL speed are measured during the data collection process. To enhance measurement precision, the measurement experiments are repeated five times. The average is taken as the result.



Figure 5. Dynamic calibration experiment: (a) GPS layout; (b) shoveling process.

4.1.2. Parameter Calibration Based on BP NNLA

(1) Factor analysis

During the material stacking section, several factors influence the state of the material stacking. These factors mainly include Poisson's ratio (A), material density (B), shear modulus (C), restitution coefficient (D), static friction coefficient (E), and dynamic friction coefficient (F). Before calibration, it is necessary to analyze the sensitivities and interactions of these factors [24]. The factors' range of fluctuation is between 0.5 and 1.5 times the baseline. Factors that have a significant impact on the stacking angle are referred to as major influencing factors. The main influencing factors are selected for analysis. In Figure 6, the factor chart shows that factors E and F have significant impacts on the stacking angle. Although factor D has a smaller impact, it has a wide practical range of fluctuation. Therefore, the factors D, E, and F are chosen as the calibration factors.

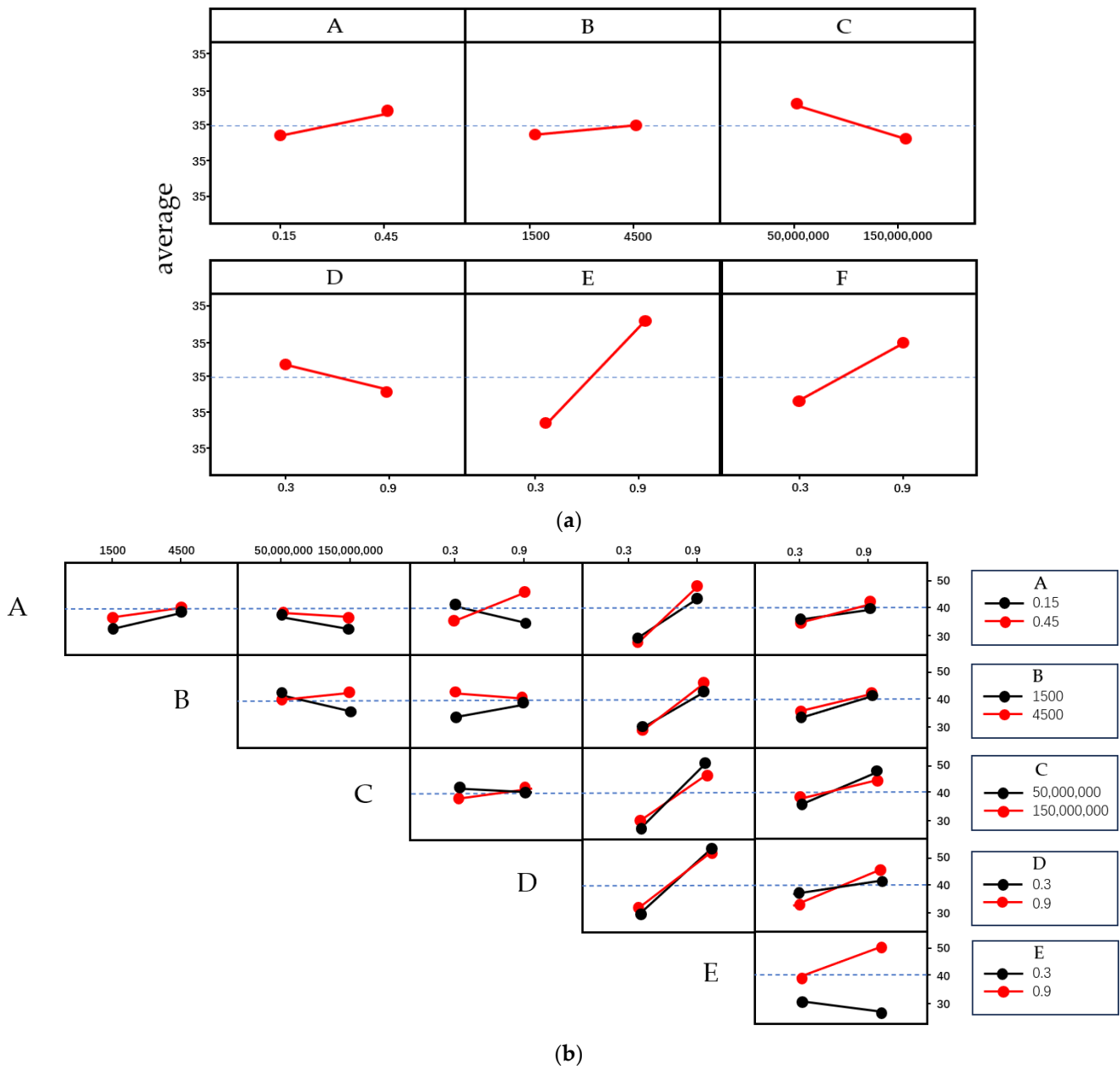


Figure 6. Factor diagram: (a) primary effect diagram of repose angle; (b) interaction diagram of repose angle.

(2) Calibration of physical parameters

Calibration is primarily divided into physical parameter calibration, density calibration, and repose-angle calibration. Physical parameter calibration requires the use of EDEM software. By means of EDEM software, density and repose angle are calibrated. For density calibration, the particle density is adjusted to the measured density [25]. Repose-angle calibration, restitution coefficient, static friction coefficient, and dynamic friction coefficient are selected as the calibration factors. The three-factor and four-level full factorial experimental design table is established, comprising a total of 64 experiments. The parameters with the smallest difference from the actual repose angle are chosen as the calibration parameters, as shown in Figure 7.

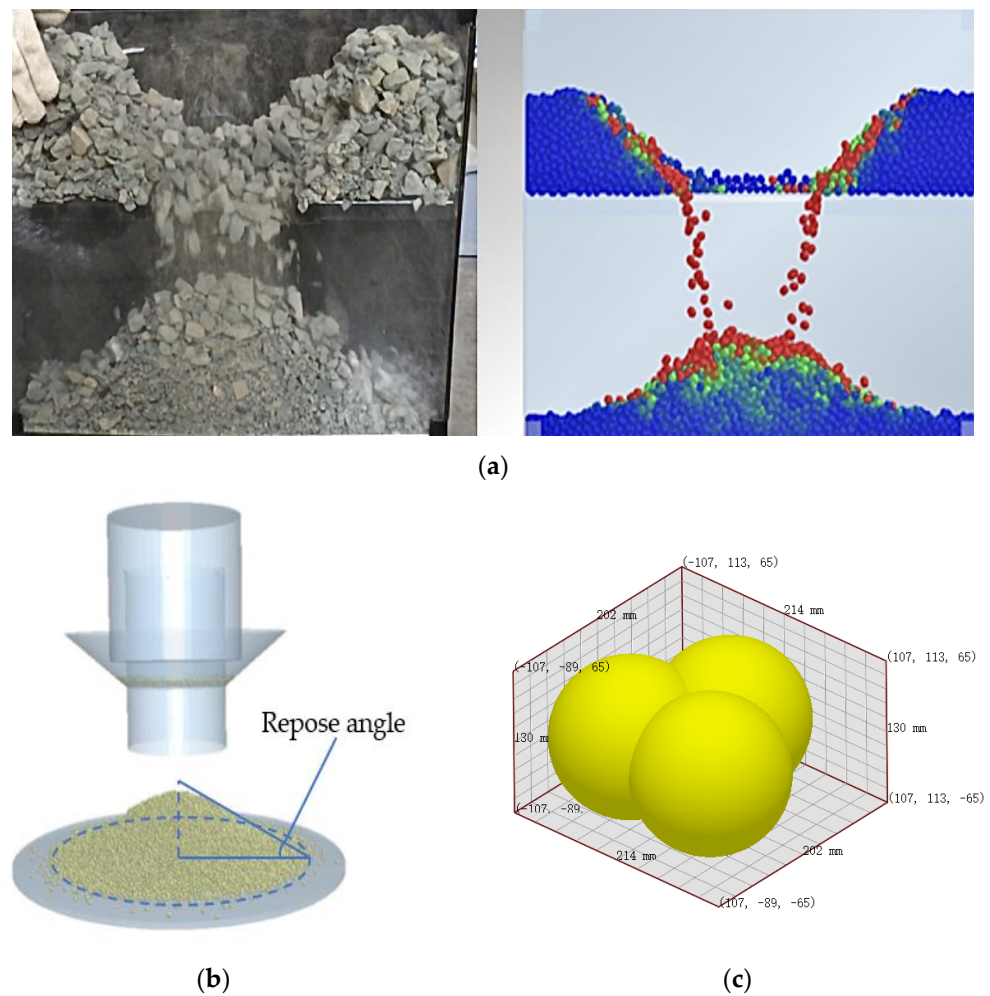


Figure 7. Physical parameter calibration model: (a) density calibration; (b) repose-angle calibration; (c) definition of material particles.

The calibration of physical parameters includes density calibration and repose-angle calibration. The density calibration process is illustrated in Figure 7a, which indicates that the actual repose density is first obtained through experiments. Subsequently, the particle density in EDEM is adjusted to match the measured density after settling [26]. The simulation process for repose-angle calibration is depicted in Figure 7b. Using the recovery coefficient, static friction coefficient, and dynamic friction coefficient as calibration factors, the three-factor, four-level, full factorial experimental design table is established, comprising 64 sets of experiments. The parameter set with the smallest deviation from the actual repose angle is chosen for the calibrated parameters. The final particle parameters are presented in Figure 8. In the EDEM simulation process, the particle shape used is depicted in Figure 7c. When using the triple sphere, the particle more closely resembles a real ore. The annotations in Figure 7c indicate the maximum values and midpoint values in each direction within the space occupied by the particle.

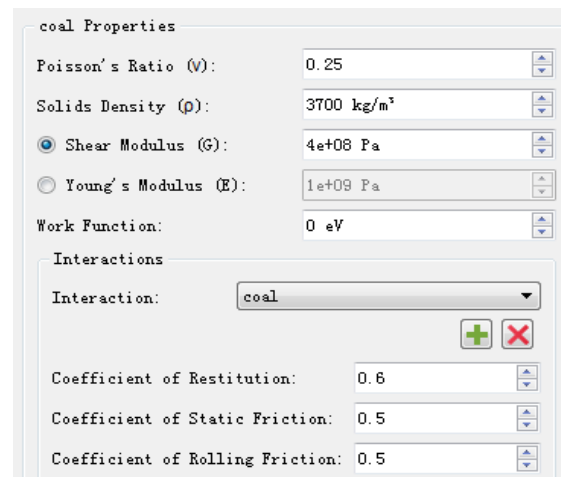


Figure 8. Definition of material properties.

(3) Mechanical Parameter Calibration

By adjusting the parameters of the bucket and the material interaction pile, the mechanical parameters are calibrated. The parameters that conform to the rules of hydraulic cylinder force are selected as the input layer nodes of the BP NNLA model [27]. Material parameters obtained from the calibration are imported to establish the material pile model. The three-factor and three-level full factorial calibration experimental design table is established. A combined simulation model is created. Measured cylinder-displacement curves and vehicle-speed variation curves are imported into the model. Hydraulic cylinder force curves are extracted. Using the BP NNLA, the curve that best matches the test hydraulic cylinder force curve is identified. The parameters corresponding to that curve are selected as the output layer. The final calibration results are obtained, as shown in Figure 9. The maximum point of hydraulic cylinder force occurs when the bucket is inserted into the material, and the hydraulic cylinder force reaches its peak when the shovel force of the bucket is at its maximum.

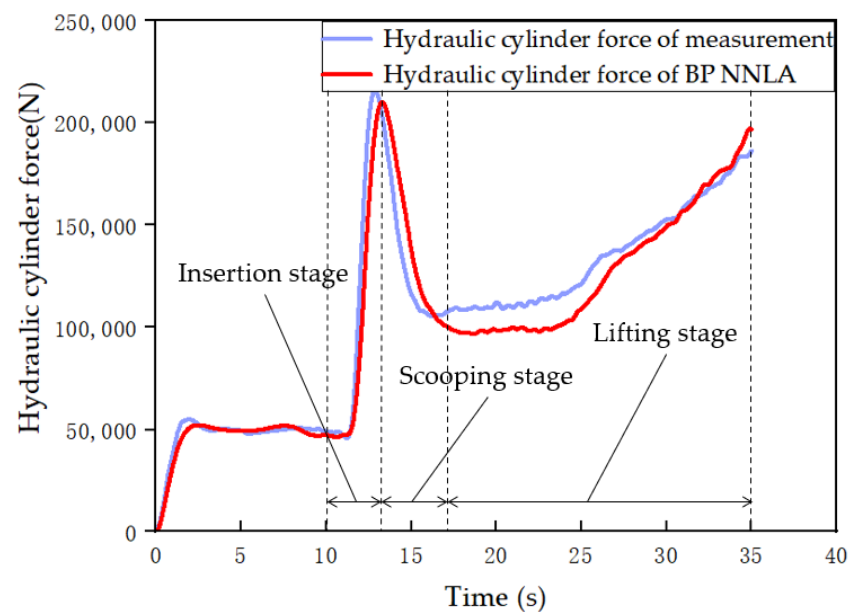


Figure 9. Variation curve of the hydraulic cylinder force.

Through the BP NNLA, the required calibration parameters are obtained. These calibrated parameters are then imported into the EDEM software. A mechanical parameter calibration model is established, as shown in Figure 10.

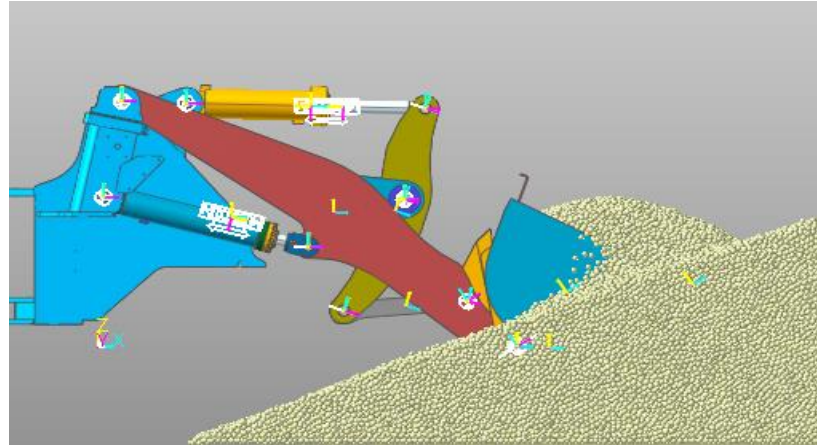


Figure 10. Mechanical parameter calibration model.

4.2. Simulation Analysis of Bucket

Based on calibrated parameters, a loading model has been established, as shown in Figure 11. This paper conducted a simulation analysis of buckets on EWLs, ranging from 3-ton to 35-ton. The predicted shovel-force determinations for EWLs all had errors below 8%. The stability of the simulation analysis was relatively high. This loading model can be used for predicting shovel force in large-tonnage EWLs. The calculated shovel force is summarized in Table 2.

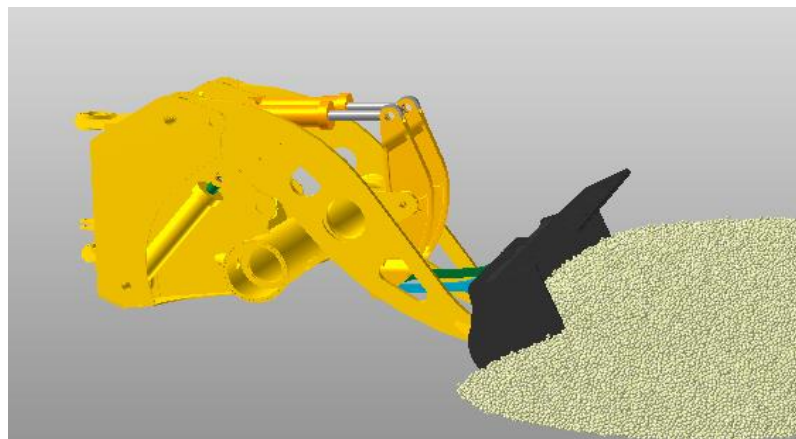


Figure 11. Bucket model of 35-ton EWL.

Table 2. Comparison and analysis of shovel forces derived from simulations.

Type of EWL /ton	Measured Shovel Force/kN	Calculated Shovel Force/kN	Error /%
3	127	129	1.57
5	160	162	1.25
7	207	211	1.4
9	270	276	2.2
12	380	395	3.95
15	420	442	5.24
35	900	968	7.56

4.3. Dynamics Matching of the Experimental EWL

The five-motor system includes four wheel-driving motors and one independent hydraulic drive motor. Different control strategies are required for various operating conditions. In November 2020, the experimental EWL model was published at the Shanghai BMW Exhibition. The experimental EWL described in this paper is the only 35-ton EWL currently available. A distributed drive configuration consisting of an engine, generator, inverter, four electric motors, and reducers was adopted. The control types depicted include mechanical control, bus control, and electrical control; the power transmission path of the experimental EWL is illustrated in Figure 12.

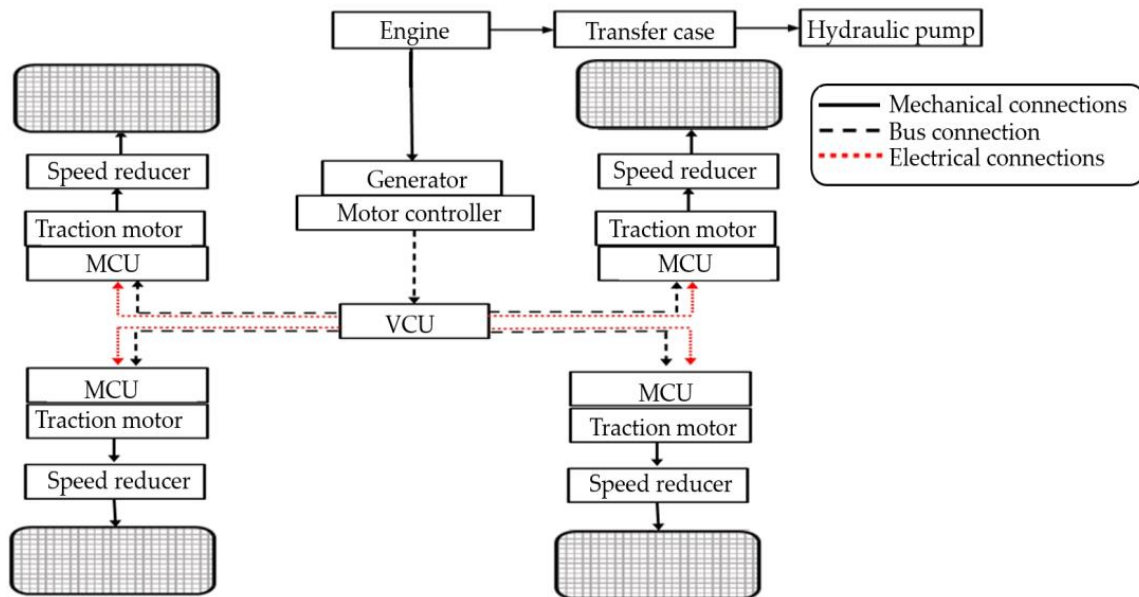


Figure 12. Power transmission path of 35-ton EWL.

The power of EWLs directly impacts the efficiency of bucket loading. The functions of EWL movement and operation are separate. To achieve the highest operational efficiency and minimize energy consumption, it is necessary to optimize the allocation of power to the EWL. The power allocation of the EWL can be optimized through the prediction of shovel force. Power allocation is determined based on the loading requirements.

4.4. Power Matching

While the shovel force of the 35-ton EWL is predicted by the loading model, the power is matched according to the power requirements for the shovel force. The typical operation of the EWL is broken down into two working conditions for power matching, with speed and torque curves as shown in Figures 13 and 14.

The condition of the EWL performing linear acceleration in first gear without a load is represented in Figure 13. Figure 13a displays the simulation curve of the speed variation during the no-load acceleration. According to empirical data, when the EWL is in first gear and accelerates in a straight line without a load, the torque is the same for all four wheels. Figure 13b shows the simulation curve of the torque variation for all four wheels during no-load acceleration.

The simulation curves of the motor torque for the front and rear wheels of the full-load EWL during first-gear linear acceleration are depicted in Figure 14. The loaded condition involves simulating materials with a 35-ton block. According to the empirical data, when the EWL is no-load and accelerates in first gear, the torque for the front two wheels is the same, and the torque for the rear two wheels is also the same. Additionally, the torque for the front two wheels is greater than that for the rear two wheels. The torque for the front wheels constitutes approximately 70–75% of the total torque for all four wheels, while

the torque for the rear wheels constitutes approximately 25–30%. Figure 14a shows the simulation curve of the torque variation for the front axle motor. When the EWL is no-load and accelerates in first gear, all four wheel torques are the same, as illustrated in Figure 14b, which presents the simulation curve of the torque variation for all four wheels during no-load acceleration.

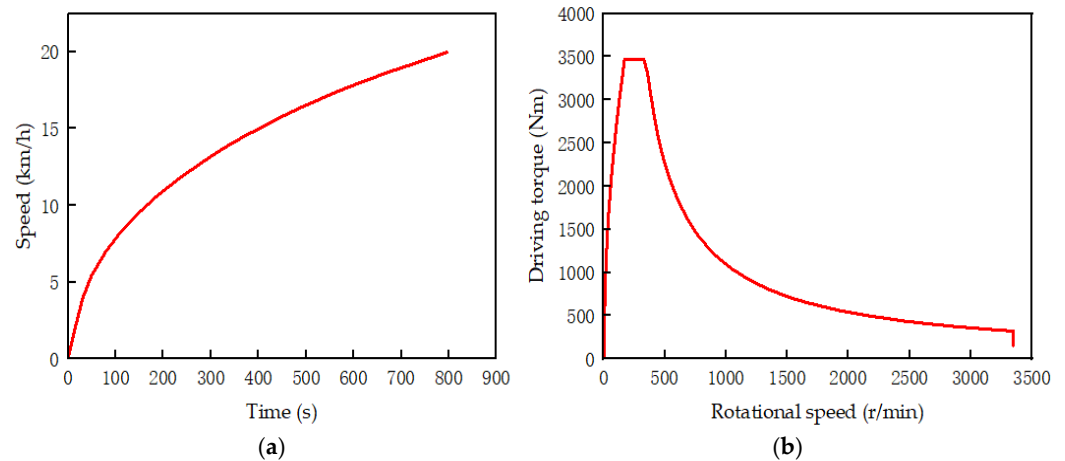


Figure 13. (a) Speed variation curve during no-load acceleration; (b) Torque variation curve during no-load acceleration.

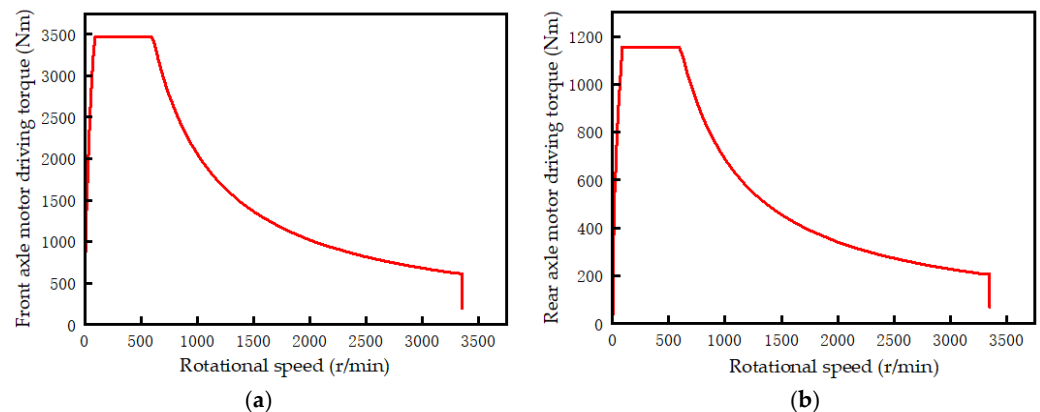


Figure 14. (a) Torque variation of front axle motors; (b) Torque variation of rear axle motors.

In typical scenarios, when the EWL is no-load, the power distribution between the front and rear axles is usually 50% for each. When the EWL is full-load, the power distribution is approximately 70–75% for the front axle and 25–30% for the rear axle. Table 3 presents the power-matching table for the EWLs. For no-load driving, the total power is 456 kW, with the sum of the power from the two front axle motors being 228 kW and the sum of the power from the two rear axle motors also being 228 kW. This results in an equal distribution of power between the front and rear axles, meeting the power-matching requirements. For full-load driving, the total power is 576 kW. The sum of the power from the two front axle motors is 426 kW, and the sum of the power from the two rear axle motors is 142 kW. In this scenario, the torque for the front wheels constitutes approximately 74% of the total torque for all four wheels, and the torque for the rear wheels constitutes approximately 26%, meeting the power-matching requirements.

Table 3. Power Matching after optimization.

Driving Conditions	Total Power/kW	Power of Front Axle Motor/kW	Power of Rear Axle Motor/kW
No-load four-wheel-drive acceleration	456	114	114
Full-load four-wheel-drive acceleration	576	213	71

Accurate prediction of the shovel force of large-tonnage loaders has enabled precise matching of the electric motors. Ultimately, by combining the dimensions of the bucket, the design of the bucket capacity, and the implementation of reduction control of shovel force, a rational torque distribution has been achieved.

5. Test of Driving Condition and Power Matching

Using a 35-ton EWL as an example, Figure 15 depicts the shovel loading test in the prototype mining area. The investigation described in this paper involved conducting comprehensive vehicle functional testing and validation, primarily focusing on the dynamic and operational performance of the EWL. The testing is performed under the condition of the straight-line movement of the EWL. During this movement, the power distribution among the four wheels of the EWL is observed. By analyzing the power curve of EWL, the adequacy of the overall power distribution for the loading requirements can be verified.

**Figure 15.** Prototype mining area shovel loading test.

(1) Straight-line Driving Conditions

The speed variation curve for unloaded first-gear linear acceleration is shown in Figure 16a. From 10 to 42 s, the driver initially presses the throttle pedal to the maximum, accelerating the entire vehicle. At 42 s, electric braking is applied, and the vehicle decelerates to a speed of 0 within 58 s.

The torque curves for all four wheels during no-load first-gear linear acceleration are depicted in Figure 16b. From Figure 16b, it can be observed that the variation trend of the motor torque for all four wheels is essentially consistent during no-load driving. The maximum motor torque is around 3500 Nm, with the sum of the torque from the front two motors being roughly equal to the sum of the torque from the rear two motors. Each set constitutes approximately 50% of the total motor torque, demonstrating the rationality of the motor-power-matching method. This validates the applicability of the proposed method.

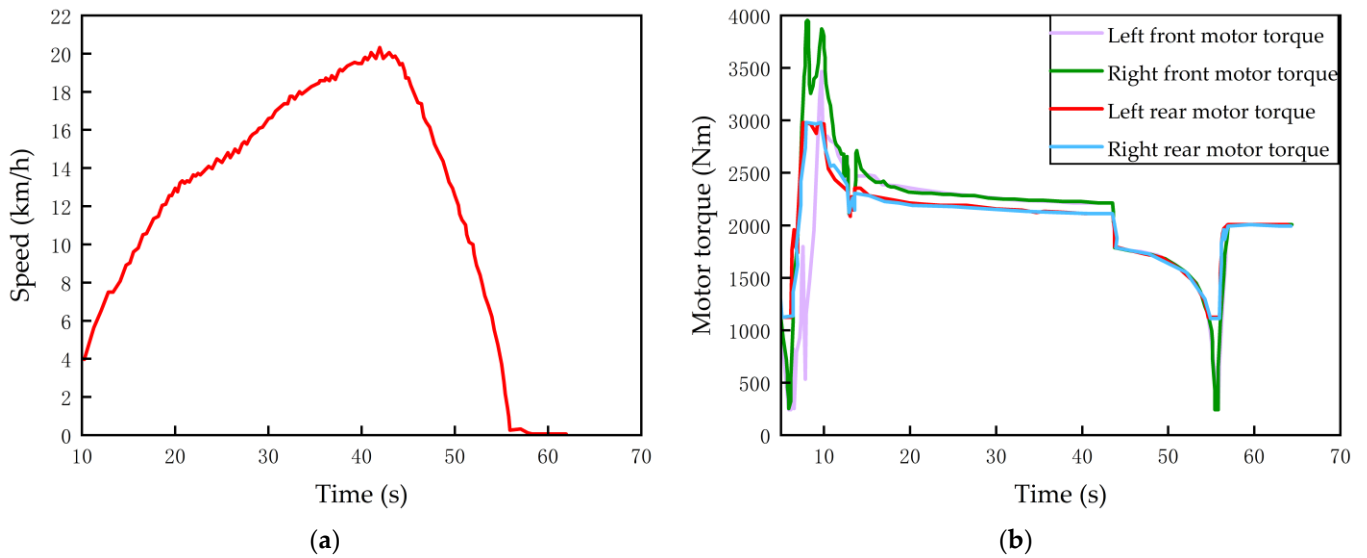


Figure 16. (a) Speed curve during linear driving process; (b) motor torque curve during linear driving process.

(2) Power-Matching Test

After calculating the torque and speed, the power of the driving motor is obtained. The power curves of the two motors are shown in Figure 17. Under no-load conditions, the maximum power for front- and rear-wheel acceleration is 112.7 kW. Under full-load conditions, the maximum power for front-wheel acceleration is 211.4 kW, and for the rear wheel, the maximum power for front-wheel acceleration is 72.1 kW. The results indicate that the power data for the front and rear motors are close, with an overall deviation of less than 2%. Power matching and control meet the practical loading requirements.

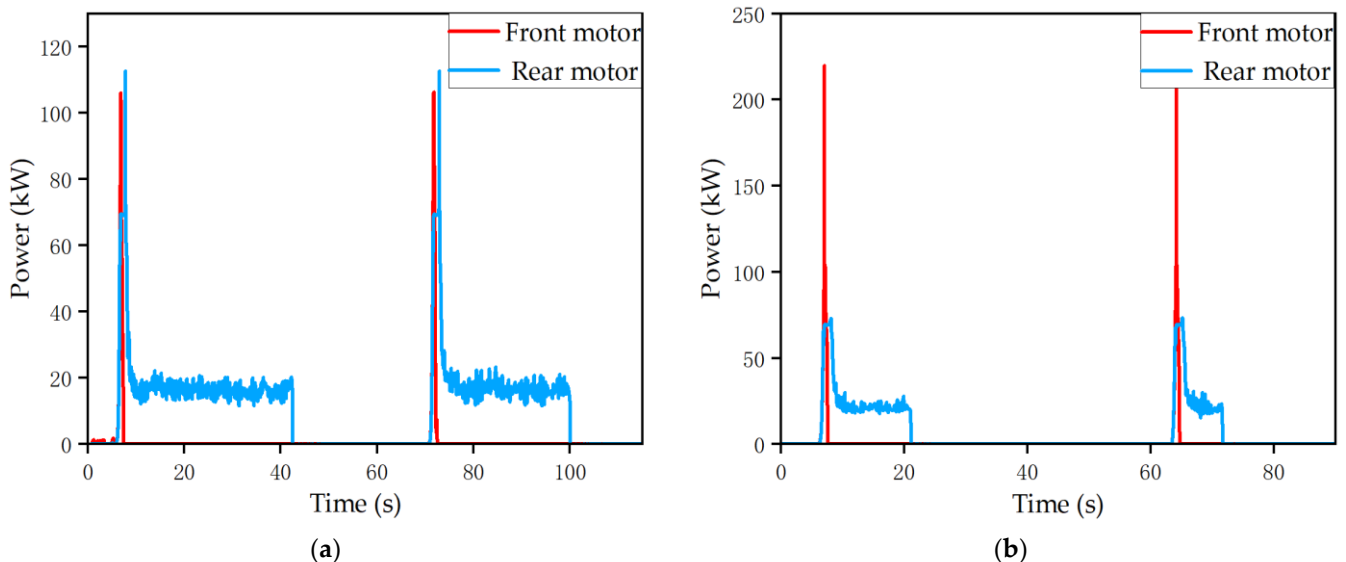


Figure 17. Power curves: (a) no-load four-wheel-drive power curve; (b) full-load four-wheel-drive power curve.

6. Discussion

In this section, the main findings of the study are discussed, in addition to its significance in both the industry and academia, and some limitations of the research are covered. This paper aims to improve the accuracy of shovel-force prediction for large-tonnage EWs to enhance their operational efficiency. Through this study, a new method for predicting

shovel force was developed, one especially designed for large-tonnage EWLs. The combination of DEM and BP NNLA demonstrated high accuracy in predicting shovel force, which can provide strong support for the design and operation of EWL. The reliability and effectiveness of this paper's findings are demonstrated in three main aspects: model verification, consideration of various factors, and comprehensive data collection. The paper validated the simulation model through experiments and considered multiple factors influencing shovel force, including material parameters, loading steps, and the physical properties of loading materials. Through static and dynamic calibration experiments, the paper extensively collected and analyzed key parameters of the shovel-force prediction model. By improving the accuracy of shovel-force prediction, it is possible to better optimize the design and operation of EWL, thereby increasing production efficiency, reducing operating costs, and enhancing competitiveness. Additionally, the optimization methods mentioned in the study for motor selection and matching can also be applied in other applications within the EWL field. This holds significant importance for other construction machinery manufacturers and industries that require efficient material handling.

Despite achieving some breakthroughs in the accurate prediction of shovel force for large-tonnage EWL in this paper, there are still some limitations. Firstly, the power matching in this paper was based on V-type operating conditions, and there is further room for optimization in real-world applications. Secondly, the discrete element simulation mainly focused on loose materials, and there might be some errors when extending the simulation to different material types. The accuracy of the simulation model can be affected by changes in actual operating conditions.

7. Conclusions

This paper focuses on the shovel force of large-tonnage EWLs, achieving precise prediction of shovel force through a combined simulation method. Additionally, the study enhances the reliability of the predicted results by validating them through experiments.

The prediction of shovel force through empirical, formula-based methods revealed significant discrepancies when compared to the actual test results, especially for large-tonnage EWL, where the error levels reached up to 30%. The empirical, formula-based methods prove to be insufficient for accurate shovel-force prediction. The combination of discrete DEM and BP NNLA offers a precise prediction of the shovel force of an EWL. Comparative analysis between the optimized shovel force obtained through this method and the actual test shovel force indicates only a small error, particularly for large-tonnage EWL, which had an error rate of 7.8%. This method proves effective in accurately predicting the shovel force for large-tonnage EWLs. Based on the predicted shovel force, this paper optimized the power matching of the large-tonnage EWLs. To validate the reliability of the optimization, the optimized large-tonnage EWL underwent straight-line movement and power-matching tests. The results demonstrate a minimal difference, one of only 2%, between the power levels of the front and rear motors of the large-tonnage EWL, meeting the operational requirements in practical scenarios.

In future work, there will be a focus on systematically studying and predicting shovel forces for various materials.

Author Contributions: Conceptualization, J.W. (Jiajie Wei) and J.W. (Jixin Wang); methodology, J.W. (Jiajie Wei); software, J.W. (Jiajie Wei) and J.Z.; validation, J.W. (Jiajie Wei) and J.Z.; formal analysis, J.W. (Jiajie Wei); investigation, J.Z. and J.W. (Jixin Wang); resources, J.Z. and J.W. (Jixin Wang); data curation, J.W. (Jiajie Wei); writing—original draft preparation, J.W. (Jiajie Wei); writing—review and editing, J.Z.; visualization, J.Z.; supervision, J.W. (Jixin Wang); project administration, J.W. (Jixin Wang); funding acquisition, J.W. (Jixin Wang). All authors have read and agreed to the published version of the manuscript.

Funding: This research was funded by the National Natural Science Foundation of China (52272434).

Institutional Review Board Statement: Not applicable.

Informed Consent Statement: Not applicable.

Data Availability Statement: The data presented in this study are available on request from the corresponding author. The data are not publicly available as the data belongs to the core information for enterprise product research and market competition.

Conflicts of Interest: The authors declare no conflict of interest.

References

1. Wang, S.; Hong, L.; Zang, B. The Path of Low-cost Carbon Peaking Change and Carbon Neutrality in China Based on The Multi-objective Model. *J. Environ. Sci. Res.* **2021**, *34*, 2044–2055.
2. Fan, D. Theoretical Analysis and Experimental Research on Hydraulic Vibration Shovel Loading of Loader. Ph.D. Thesis, Jilin University, Jilin, China, 2006.
3. Li, R.; Xu, W.; Li, B. Research on Discrete Element Method for Loading Shovel Bucket Loading Resistance. *J. Guangxi Univ. Sci. Technol.* **2017**, *28*, 77–82.
4. Chen, Y.; Li, B.; Du, X. The Study of Loader Shovel Bucket Tooth Number on the Properties of Shovel Loading Impact. *J. Constr. Mach.* **2016**, 55–58. [[CrossRef](#)]
5. Ding, Z.; Wu, X.; Chen, C.; Yuan, X. Magnetic Field Analysis of Surface-Mounted Permanent Magnet Motors Based on an Improved Conformal Mapping Method. *IEEE Trans. Ind. Appl.* **2022**, *59*, 1689. [[CrossRef](#)]
6. Yang, M.; Wang, Y.; Liang, Y.; Wang, C. A New Approach to System Design Optimization of Underwater Gliders. *IEEE/ASME Trans. Mechatron.* **2022**, *27*, 3494–3505. [[CrossRef](#)]
7. Bai, X.; He, Y.; Xu, M. Low-Thrust Reconfiguration Strategy and Optimization for Formation Flying Using Jordan Normal Form. *IEEE Trans. Aerosp. Electron. Syst.* **2021**, *57*, 3279–3295. [[CrossRef](#)]
8. Shi, M.; Lv, L.; Xu, L. A Multi-fidelity Surrogate Model Based on Extreme Support Vector Regression: Fusing Different Fidelity Data for Engineering Design. *J. Eng. Comput.* **2023**, *13*, 0264–4401. [[CrossRef](#)]
9. Liu, L.; Wu, Y.; Wang, Y.; Wu, J.; Fu, S. Exploration of environmentally friendly marine power technology—Ammonia/diesel stratified injection. *J. Clean. Prod.* **2022**, *380*, 135014. [[CrossRef](#)]
10. Bai, X.; Zhang, Z.; Shi, H.; Luo, Z.; Li, T. Identification of subsurface mesoscale crack in full ceramic ball bearings based on strain energy theory. *Appl. Sci.* **2023**, *13*, 7783. [[CrossRef](#)]
11. Li, T.; Shi, H.; Bai, X.; Zheng, K.; Bin, G. Early Performance Degradation of Ceramic Bearings by a Twin-driven Model. *Mech. Syst. Signal Process.* **2023**, *204*, 110826. [[CrossRef](#)]
12. Liao, K.; Lu, D.; Wang, M.; Yang, J. A Low-Pass Virtual Filter for Output Power Smoothing of Wind Energy Conversion Systems. *IEEE Trans. Ind. Electron.* **2022**, *69*, 12874–12885. [[CrossRef](#)]
13. Li, Z. Research on Performance Improvement of the 3-Tonnage Loader Bucket. Ph.D. Thesis, Shandong University, Jinan, China, 2016.
14. Zauner, M.; Altenberger, F.; Knapp, H.; Kozek, M. Phase Independent Finding and Classification of Wheel Loader Work-cycles. *J. Autom. Constr.* **2020**, *109*, 102962. [[CrossRef](#)]
15. Myers, R.H. Response Surface Methodology: A Retrospective and Literature Survey. *J. Qual. Technol.* **2004**, *36*, 53–77. [[CrossRef](#)]
16. Satpathy, S.D.; Bhattacharyya, B.K. How and Where to Use Super-capacitors Effectively, an Integration of Review of Past and New Characterization Work on Super-capacitors. *J. Energy Storage* **2020**, *27*, 101044. [[CrossRef](#)]
17. Zhao, Z.; Gu, J.; Yu, Z. Four-wheel Drive Hybrid Electric Vehicle Drives Anti-skid Control Research. *J. Mech. Eng.* **2011**, *47*, 83–98. [[CrossRef](#)]
18. Coetzee, C.; Els, D. The Numerical Modelling of Excavator Bucket Filling Using DEM. *J. Terr. Mech.* **2009**, *46*, 217–227. [[CrossRef](#)]
19. Dixon, J.; Nakashima, I.; Arcos, E.F.; Ortuzar, M. Electric Vehicle Using a Combination of Ultracapacitors and ZEBRA Battery. *Ind. Electron.* **2010**, *57*, 943–949. [[CrossRef](#)]
20. Zeng, Q.; Qin, S.; Zhao, T.; Wang, X. Loading Machine Bucket Loading Process Force Analysis. *J. Constr. Mach.* **2011**, *42*, 18–21+101–102.
21. Zhang, R.; Huang, M. Research on Dynamic Weighing Data Processing Methods for Loader Material Loading. *J. Electromechanical Eng.* **2021**, *38*, 1486–1493.
22. Wang, G. *Discrete Element Method and Its Practice on EDEM. M*; Northwestern Polytechnical University Press: Xi'an, China, 2010.
23. Sagir, A.M.; Asthasivam, S. The Use of Artificial Neural Network and Multiple Linear Regressions for Stock Market Forecasting. *Mat. Malays. J. Ind. Appl. Math.* **2017**, *33*, 1–10. [[CrossRef](#)]
24. Favler, J.; Industri, N. *Application of DEM: Opportunities and Challenges*; DEMOT: Brisbane, Australia, 2007.
25. Cleary, P.W. Industrial Particle Flow Modeling Using Discrete Element Method. *J. Eng. Comput.* **2009**, *26*, 698–743. [[CrossRef](#)]
26. Lin, G.; Li, A. Study on The Value and Method of Determining the Key Factors of Shovel Force. *J. Northeast. Univ.* **2010**, *31*, 1761–1764.
27. Yang, C.; Liu, H. Causes of Loader Tire Slippage and Countermeasures. *J. Constr. Mach.* **2008**, *57*, 23–24.

Disclaimer/Publisher's Note: The statements, opinions and data contained in all publications are solely those of the individual author(s) and contributor(s) and not of MDPI and/or the editor(s). MDPI and/or the editor(s) disclaim responsibility for any injury to people or property resulting from any ideas, methods, instructions or products referred to in the content.